JCIM JOURNAL OF CHEMICAL INFORMATION AND MODELING

pubs.acs.org/jcim Article

Light-Induced Change of Arginine Conformation Modulates the Rate of Adenosine Triphosphate to Cyclic Adenosine Monophosphate Conversion in the Optogenetic System Containing Photoactivated Adenylyl Cyclase

Maria G. Khrenova,* Anna M. Kulakova, and Alexander V. Nemukhin*

Cite This: *J. Chem. Inf. Model.* 2021, 61, 1215−1225

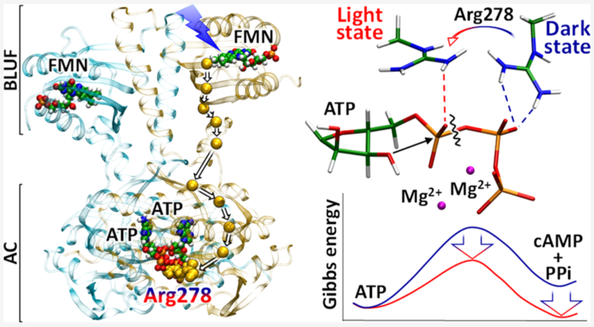

ABSTRACT: We report the first computational characterization of an optogenetic system composed of two photosensing BLUF (blue light sensor using flavin adenine dinucleotide) domains and two catalytic adenylyl cyclase (AC) domains. Conversion of adenosine triphosphate (ATP) to the reaction products, cyclic adenosine monophosphate (cAMP) and pyrophosphate (PPi), catalyzed by ACs initiated by excitation in photosensing domains has emerged in the focus of modern optogenetic applications because of the request in photoregulated enzymes that modulate cellular concentrations of signaling messengers. The photoactivated AC from the soil bacterium *Beggiatoa* sp. (bPAC) is an important model showing a considerable increase in the ATP to cAMP conversion rate in the catalytic domain after the illumination of the BLUF domain. The 1 μs classical molecular dynamics simulations reveal that the activation of the BLUF domain leading to tautomerization of Gln49 in the chromophore-binding pocket results in switching of the position of the side chain of Arg278 in the active site of AC. Allosteric signal transmission pathways between Gln49 from BLUF and Arg278 from AC were revealed by the dynamical network analysis. The Gibbs energy profiles of the ATP → cAMP + PPi reaction computed using QM(DFT(ωB97X-D3/6-31G**))/MM(CHARMM) molecular dynamics simulations for both Arg278 conformations in AC clarify the reaction mechanism. In the light-activated system, the corresponding arginine conformation stabilizes the pentacoordinated phosphorus of the α-phosphate group in the transition state, thus lowering the activation energy. Simulations of the bPAC system with the Tyr7Phe replacement in the BLUF demonstrate occurrence of both arginine conformations in an equal ratio, explaining the experimentally observed intermediate catalytic activity of the bPAC-Y7F variant as compared with the dark and light states of the wild-type bPAC.

■ INTRODUCTION

Photoreceptor protein domains coupled with enzyme domains form powerful light-regulated biocatalysts utilized in optogenetics.[1,2] Recently, the photoregulated reaction of conversion of adenosine triphosphate (ATP) to cyclic adenosine monophosphate (cAMP) and pyrophosphate (PPi), illustrated in Figure 1, has emerged in the focus of modern optogenetic applications as a tool to modulate cellular concentration of signaling messengers.[3−5]

This reaction catalyzed by adenylyl cyclases (ACs) is one of the most important biochemical transformations by itself.[7−9] In particular, ACs are essential in the signaling in GPCR (G protein-coupled receptors).[10,11] It seems deceptively simple: the P^A-O^{3A} bond in ATP is cleaved and the $P^A-O^{3'}$ bond is formed, thus resulting in the cAMP and PPi reaction products; however, mechanistic details are important, as discussed below.

The AC domains combined with the photosensing domains comprise photoregulated ACs. In particular, the BLUF (blue light sensor using flavin adenine dinucleotide),[12−20] rhodopsin,[21] and cyanobacteriochrome[22] photoreceptor proteins are considered as photosensing partners in optogenetic systems. In this work, we focus on the photoactivated AC (PAC) from the soil bacterium *Beggiatoa* sp. (bPAC)[16,18] because it shows a remarkable acceleration of the ATP → cAMP reaction in the catalytic domains upon light illumination of the photosensing BLUF domains. According to refs,[17,18] the photoactivation results in the ~300 fold increase of the ATP to cAMP conversion rate as compared with only up to 20 times photoinduced acceleration in other PACs.[17,20]

Received: November 11, 2020
Published: March 8, 2021

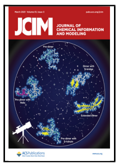

https://dx.doi.org/10.1021/acs.jcim.0c01308

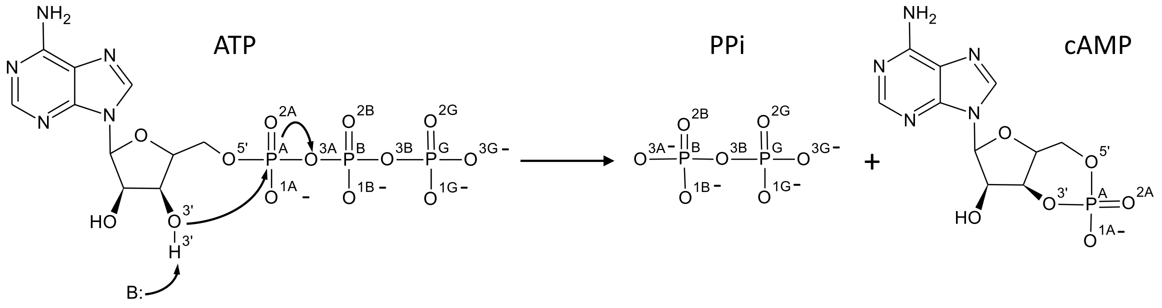

Figure 1. Reaction of the ATP to cAMP conversion catalyzed by ACs. Names of atoms are given according to the IUPAC recommendations.[6]

The molecular mechanism of the light-induced acceleration of the ATP → cAMP chemical reaction in PACs remains uncovered. Lindner et al.[17] reported the results of structural, kinetic, and mutational studies in bPAC, which were interpreted on the base of the obtained crystal structures of the protein in the dark and light-illuminated (shortly, light) states of the BLUF domains containing flavin mononucleotide (FMN) cofactors but bearing no substrates or substrate analogues in the AC domains. These results[17] are consistent with those obtained in studies of the homologous OaPAC protein[14,15,23] in respect that small structural changes occur upon dark to light transition. The authors of ref 17 assumed that highly conserved residues of the BLUF domain, Tyr7 and Gln49, the kink in $\beta4_{\mathrm{BLUF}}$, and the C-terminal BLUF capping helix were involved in the signaling pathway. Stierl et al.[24] described the role of point mutations within the BLUF domain in bPAC. In particular, the protein complex called as bPAC-Y7F (i.e., that with the Tyr7Phe mutation) results in locking the BLUF domain in the so-called pseudolit state.[25] The bPAC-Y7F shows intermediate catalytic activity of the AC domain, as compared with the dark and light states of the wild-type bPAC.[17,24]

Importantly, the authors of all papers on PACs[14,15,17,24] focused almost entirely on the processes in the light-sensitive BLUF domain but not on the mechanism of chemical reactions of the ATP to cAMP conversion in the catalytic domain. The only available information on the ATP → cAMP + PPi reaction in bPAC is the steady-state catalytic rate constant[16,17] and the K_M value.[16] The reported rate constant in the dark state is $0.008 \pm 0.001\ \mathrm{s}^{-1}$, whereas it increases to $2.6 \pm 0.3\ \mathrm{s}^{-1}$ under constant blue light illumination.[17] More precisely, the samples were illuminated with a collimated royal blue LED at 7 $\mathrm{mW/cm}^2$ to produce the light state.[17] In this respect, studies of the structurally similar mammalian ACs (mACs) can provide additional data. Reference 26 reports the rate of the chemical reaction inside the protein matrix 59 s^{-1} following the fitting of rate constants in a complex kinetic model of mAC inhibition. The steady-state experiments[26] were performed, resulting in the $V_{\max}$ and K_m parameters of the Michaelis−Menten scheme for the forward (ATP to cAMP) and backward (cAMP to ATP) reactions. Additionally, the set of inhibition constants K_i was measured. To gain a more detailed characterization as compared with the steady-state $V_{\max} = 100 \pm 30\ \mathrm{s}^{-1}$, a complex kinetic scheme was proposed and the corresponding equations were solved together with the experimental data. For the goals of our work, it is important to note that ref 27 emphasizes the effect of the conserved arginine residue Arg1029 in mAC (analogous to Arg278 in bPAC). It was shown that its mutation to Ala resulted in more than 10-fold decrease in the reaction rate, keeping the catalytic activity.[27] At the same time, this replacement did not affect the binding affinity, that is, did not change the K_M value.[27] The X-ray study (PDB ID: 1CJK[27]) demonstrated that the arginine side chain was located closely to the α-phosphate group and might stabilize the transition state of reaction.[27] Following these findings, Lindner et al.[17] tentatively assumed that the corresponding residue Arg278 in the catalytic domain in bPAC might play a role. Their evidence demonstrates a very limited knowledge on the mechanism of the ATP to cAMP conversion in bPAC.

Computer simulations can deepen the understanding of molecular processes both in photosensing and catalytic domains. In particular, details of transformations upon light excitation in the BLUF domains originally revealed in simulations[28] and confirmed later[29−33] show that the side chain of the conserved glutamine (such as Gln49 in bPAC) in the chromophore-binding pocket undergoes amide−imide tautomerization. The mechanism of the ATP → cAMP conversion in the active sites of ACs, including mammalian and bacterial ACs unbound to other protein domains, was modeled in infrequent computational papers.[34−37] The latter studies employed different versions of the quantum chemistry and quantum mechanics/molecular mechanics (QM/MM) approaches to characterize the reaction route from reactants to products (Figure 1) in the active sites of the corresponding enzymes, showing somewhat diversity in conclusions. No theoretical simulations revealing the mechanism of photo-activation of catalysis in AC have been reported for bPAC and for any other PAC systems.

The aim of this work is to establish the atom-level mechanism of the ATP to cAMP conversion in bPAC and to reveal the origin of the acceleration of this reaction upon blue light illumination of the protein complex. After construction of an all-atom model molecular system of bPAC, we apply modern approaches based on molecular dynamics (MD) simulations. We recognize conformational changes in this optogenetic complex following transition from the dark to light states and identify the key role of switching between conformations of the Arg278 side chain in the AC active site. We find that this switching is important in the wild-type bPAC and in its bPAC-Y7F variant with an intermediate catalytic activity. We compute and compare the Gibbs energy profiles of the ATP → cAMP reaction in the dark and light states of bPAC using MD with the QM/MM (QM(DFT-(ωB97X-D3/6-31G**))/MM) potentials. We also consider qualitative aspects of the chemical reaction in this protein environment by analyzing the relevant electron density-based descriptors.[38−40]

The outline of the paper is as follows. After the methodology section, we describe the construction of model systems and the results of large-scale classical MD simulations in both dark and light states of the wild-type bPAC and bPAC-Y7F mutant followed by the dynamical network analysis that clarifies the signal transmission path from the flavin-binding pocket in BLUF to Arg278 in the AC domain. Next, we describe the results obtained with the *ab initio*-type QM/MM MD calculations of the Gibbs energy profiles in the dark and light states. This allowed us to formulate for the first time a consistent picture of photoexcitation and enzymatic processes in bPAC.

■ METHODS

The crystal structure (PDB ID: 5M2A[17]) of the bPAC dimer with the FMN cofactors in the photoreceptor domains but without the substrate or substrate analogues in the catalytic domains was used as a source of initial coordinates of heavy atoms. Amino acid residues, which were poorly resolved in the X-ray analysis, were added using the data on the primary sequence (UniProt A7BT71). Hydrogen atoms were added using the Reduce program[41] to reproduce the protonation states of amino acids at neutral pH. The ATP molecule was manually added to each subunit of bPAC following motifs of the crystal structures of complexes of human AC with ATP (PDB ID: 4USW[42]) and with the guanosine triphosphate (GTP) analogue GTPγS (PDB ID: 1CJK[27]). Thus, the constructed model was assigned to the dark state of the protein complex. The light state of bPAC was obtained from the dark state by replacing the amide group of the Gln49 side chain by the imide group, that is, assuming tautomerization of the Gln49 side chain.[28,29,33] The bPAC-Y7F mutant was constructed from the dark-state model system replacing Tyr7 by phenylalanine. The flavin molecule occurs in the ground electronic state; correspondingly, the same partial atomic charges are utilized for its atoms in all considered models. All these model systems were solvated in a rectangular water box with the dimension of 111 × 97 × 130 Å^3 and properly neutralized. Despite the large system size, we utilized all-atom force fields: CHARMM36[43,44] for the protein, ATP, and the magnesium ions and the TIP3P[45] for water molecules. Force field parameters for the FMN molecule were obtained from the CGenFF server[46] and additionally optimized.[47] Parameters of the imide form of glutamine were taken from our previous work.[48]

VMD software[49] was used for preparation of all considered systems and for analysis of MD trajectories. All MD calculations were carried out with a 1 fs integration time step using the NAMD 2.13 software package.[50] The *NPT* ensemble was utilized with the $P = 1$ atm and $T = 300$ K with the pressure and temperature controlled using the Nosé–Hoover barostat and Langevin thermostat, respectively. The cutoff distances were 12 Å for both electrostatic and van der Waals interactions with switching to the smoothing function at 10 Å.

Preparation of bPAC complexes for the production runs consisted of two steps: equilibration of solvating water shells and equilibration of the entire system. In the first step, the 1 ns molecular dynamic simulation was performed keeping the coordinates of the protein, magnesium ions, ATP, and FMN fixed. The second step was a 20 ns MD run with no constraints or restraints. The representative frame from the last 5 ns of this trajectory was used to select coordinates for further MD simulations. Next, a 200 ns simulation was performed. We selected four frames with the most distinct structures as estimated from the RMSD values and utilized them for additional four 200 ns MD runs. The total length of the production runs was 1 μs for each model. To avoid accumulation of the computational errors and to gain better sampling of the conformational space, we executed sets of the trajectories with tens of nanoseconds each, as suggested in ref 51.

Dynamical network analysis[52] was utilized to dissect the signaling pathways from photosensing to catalytic domains in the bPAC dimer. According to this approach, a network is defined as a set of nodes connected by edges. In this work, every amino acid was represented by a single node; the ATP and FMN moieties were divided into two nodes each. Any two nodes (except the neighbors) were connected by an edge if the distance between any pair of atoms of the respective residues was less than 4 Å for more than 75% of the simulation time. Covariance and correlation matrices for dynamical network analysis were calculated with the CARMA program.[53]

The QM/MM MD simulations with the *ab initio*-type potentials in QM were performed to study the reaction mechanism in the dark and light states. We exploited the NAMD program for MD calculations and the NAMD interface[54] between the TeraChem program[55] for calculating forces in QM and the NAMD program for calculating forces in MM.[50] The starting points for the QM/MM MD simulations were obtained from the representative frames of the classical MD trajectories of the dark and light states. The QM subsystem was described at the ωB97X-D3/6-31G** Kohn–Sham DFT level. The rest of the system, that is, the MM part, was described with the same force field parameters as in the classical MD simulations. The 5 ps QM/MM MD pre-equilibration of the ES (enzyme–substrate) complexes was performed. Then, the 10 ps production runs of the ES complexes were executed. The ES to EP (enzyme–product) transition was calculated within the umbrella sampling approach followed by the umbrella integration analysis. The reaction coordinate, ξ, was set as a difference of two distances, $d(\mathrm{O}^{3'}\cdots\mathrm{P}^{\mathrm{A}})$ and $d(\mathrm{P}^{\mathrm{A}}\cdots\mathrm{O}^{3\mathrm{A}})$ being positive in ES and negative in EP regions. The force constant, K, of the harmonic potential $K(\xi - \xi_0)^2$ was set to 40 kcal/mol/Å^2. These potentials were centered at the respective ξ_0 values with the 0.3 Å increment with the ranges depending on the model system. In the light state, we performed nine simulations with the biasing potentials varying from −1.2 to 1.2 Å. In the dark state, we performed 14 simulations with ξ_0 from −2.4 to 1.5 Å. First, 0.5 ps from each 10 ps MD run was excluded from the statistical analysis. After simulation of the reaction energy profiles, additional 10 ps runs for each EP complexes were performed.

The Laplacian of the electron density, $\nabla^2\rho(\mathbf{r})$,[38,56] was calculated at different frames of the QM/MM MD trajectory of the ES complex to discriminate reactive and nonreactive species. Previous studies[39,40,57,58] demonstrate that this approach is a proper tool to visualize the activation in the nucleophilic attack step. In the molecular systems, the areas of the local electronic charge concentration regions with $\nabla^2\rho(\mathbf{r}) < 0$ (electrophilic sites) and electronic charge depletion areas with $\nabla^2\rho(\mathbf{r}) > 0$ (nucleophilic sites) are formed. Analysis of $\nabla^2\rho(\mathbf{r})$ in the plane formed by the nucleophilic $\mathrm{O}^{3'}$ atom and the P^{A}–$\mathrm{O}^{3\mathrm{A}}$ bond provides easily visible images, which help us to discriminate conformations favorable and unfavorable for the chemical reaction. Namely, the electron lone pair on the $\mathrm{O}^{3'}$ atom is oriented toward the electrophilic P^{A} if the ATP is prepared for the chemical reaction. Electron density analysis was performed in the Multiwfn program package.[59]

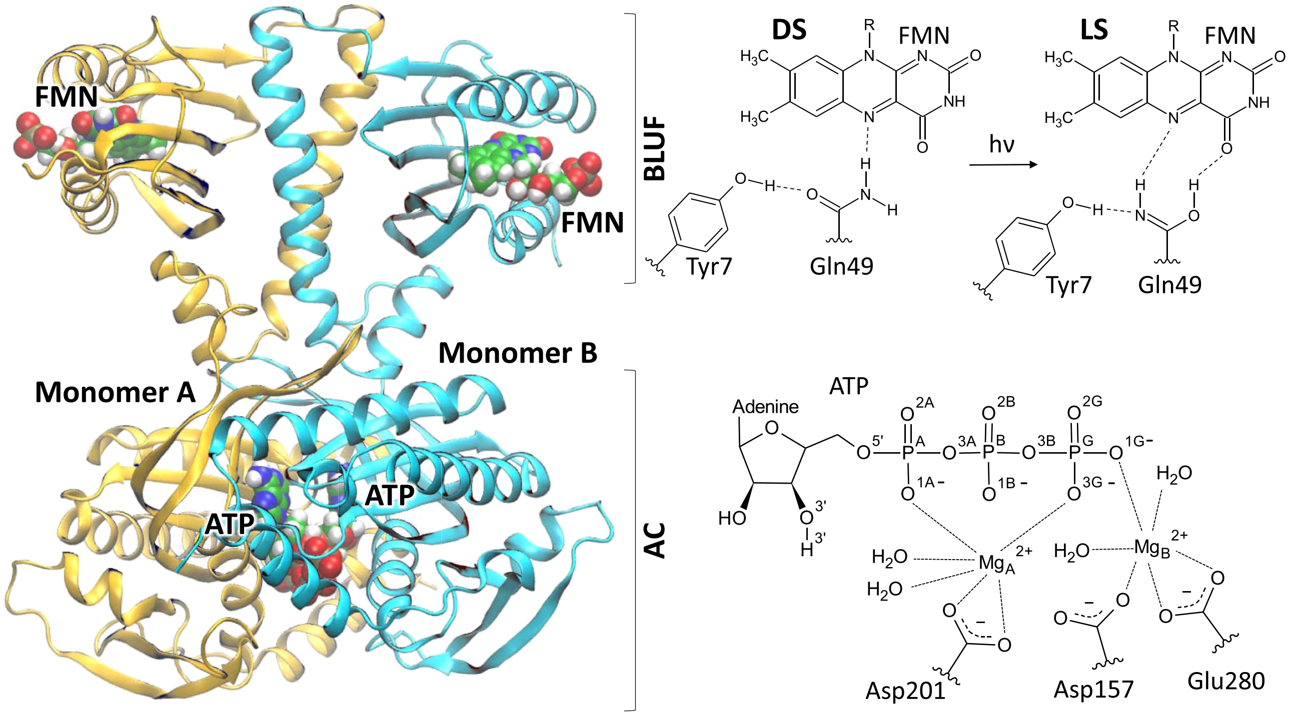

Figure 2. Left side illustrates a general view on the computationally derived bPAC dimer. Monomer A is shown in yellow, monomer B—in cyan. The FMN and ATP molecules are shown as space-filling spheres. Here and in all figures given below, the atom colors are the following: carbon in green, nitrogen in blue, phosphorus in orange, magnesium in magenta, oxygen in red, and hydrogen in white. The right side illustrates the photoinduced transformations in the BLUF domain (upper panel) and the active site in AC (lower panel). Here and in the next figures, carbon—green, oxygen—red, nitrogen—blue, hydrogen—white, phosphorus—orange, and magnesium—magenta.

■ RESULTS AND DISCUSSION

Computationally Derived Structures of bPAC. As described in the Methods, we constructed the systems, modeling the bPAC dimer composed of two BLUF domains with the FMN molecules in the chromophore-containing pockets and two AC domains containing the ATP molecules. Model systems correspond to the dark (DS) and light (LS) states of the wild-type bPAC and to the bPAC-Y7F variant. A general view on the obtained complex is illustrated in Figure 2. The panels in the right side in Figure 2 show some patterns in the chromophore-containing pocket in the BLUF and in the active site in AC.

Two important residues Tyr7 and Gln49 are located near the FMN cofactor in the BLUF (Figure 2). In the wild-type BLUF, light illumination initiates a photoreaction that comprises the electron and proton transfer to the isoalloxazine ring of the FMN molecule.[32] Similar processes happen during the redox reactions with the flavin molecule (see, e.g., ref 60). After relaxation, the light state is formed, the FMN molecule returns to its oxidized state, and the proton rearrangement takes place. As a result of this process, the Gln49 side chain tautomerizes and rotates around the single C−C bond (Figure 2).[28,29,33] Therefore, in our simulations, the dark and light states differ in the conformation of the Gln49 side chain. In the bPAC-Y7F mutant, the photoreaction is locked, and the Gln49 side chain remains in the same amide form independent of illumination.[17]

The active site in AC domains (Figure 2) carries two magnesium cations; both of them are hexacoordinated with water molecules, the oxygen atoms of ATP, and the side chains of the glutamate and aspartate residues, in agreement with the available structures of the mammalian ACs complexed with the substrate or its analogues.[27,42]

We analyzed the dynamical behavior of three model systems, DS, LS, and bPAC-Y7F, as obtained in the 1 μs MD trajectories. First, the comparison of the constructed models with the available X-ray data was performed. The protein coordinates from the MD snapshots were aligned to the corresponding crystal structures. Four structures are available for the DS, PDB ID 5M27, 5M2A, 5MBC, and 5MBB.[17] The RMSD values for the heavy atoms of proteins calculated for the corresponding structures were 4.2−4.3 Å depending on the particular crystal. For the LS, comparison with the PDB ID 5MBD and 5MBE[17] was performed. The RMSD values are 4.5 and 4.8 Å, respectively. Comparison with the PDB ID 5NBY and 5MBK[17] was performed for the Y7F mutant; the RMSD values were 3.3 Å for both structures.

Next, we paid major attention to the individual residues that might be responsible for the changes of the ATP → cAMP reaction rate, that is, to those located in the active site of AC or in the immediate vicinity of the latter. The most important conclusion refers to the Arg278 conformations, which differ significantly in the considered model system. This means that the arginine side chain adopts two different conformations in the dark and light states of the complex. Distributions of the χ dihedral angle (see Figure 3), corresponding to the C^A−C^B−C^G−C^D fragment of the arginine side chain, allow us to characterize these conformations. In the DS (blue line in Figure 3), values of χ are predominantly negative with the distribution maximum located at around −65°. In the LS (red line in Figure 3), this population is minor, and the vast majority of conformations correspond to the χ values around 70°. DS-type conformations with the negative χ values

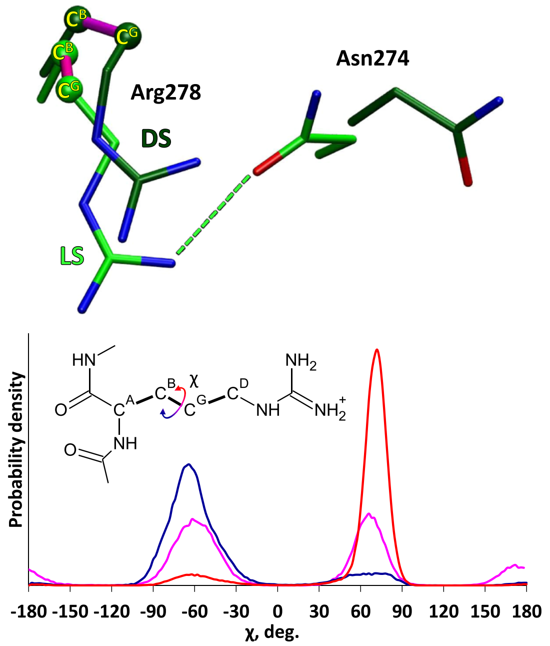

Figure 3. Upper panel: Alignment of the major conformations of the Arg278 and Asn274 side chains in the DS (carbon in dark green) and LS (carbon in light green). The C^G-C^B covalent bonds in Arg278 are highlighted in magenta and the corresponding atoms are shown in ball representation. The hydrogen bond is shown as a green dashed line. Lower panel: The χ dihedral angle distributions in the Arg278 side chain along classical MD trajectories in DS (blue), LS (red), and bPAC-Y7F (magenta) model systems.

promote the hydrogen bond interaction between the guanidinium group of Arg278 and the O^{1B} atom of the ATP β-phosphate group, as explained in detail below. If χ is around 70°, the side chain of Arg278 interacts with the O^{1A} atom of the ATP α-phosphate group. This conformation should be more favorable for the chemical reaction because the P−O bond cleavage in nucleotide phosphates is normally facilitated by an arginine residue due to stabilization of the transition state and corresponding lowering of activation energy barriers.[61] The computed distribution for the bPAC-Y7F system (magenta line in Figure 3) provides further support to the hypothesis of the role of Arg278 in the photoinduced acceleration of the reaction rate. We see the presence of both arginine conformations in an equal ratio, which is consistent with the experimentally observed[17] intermediate catalytic activity of the bPAC-Y7F variant as compared with the dark and light states of the wild-type bPAC.

Signal Transmission from the Photosensing Domain to the Catalytic Domain. We analyze allosteric signal transmission pathways from Gln49 to Arg278 in the dark and light states of the wild-type bPAC and identify amino acid residues that are involved in the signaling paths more frequently (Figure 4). The Gln49, playing a critical role in BLUF domain photoinduced processes, is hydrogen-bonded to the FMN; its side chain tautomerizes during the photoreaction.[28,29,33] The signal proceeds to the neighboring β-sheets, $\beta1_{BLUF}$ (Tyr7) and $\beta4_{BLUF}$ (Leu75) (Figure 4). The importance of Tyr7, which is involved in the signaling pathway, is demonstrated in the experimental study on the light-regulated AC activity in mutated bPAC variants.[17] It is in line with other experimental results on the mutational analysis of the BLUF-containing protein PixD.[25] The Leu75 is a conservative residue among BLUF domains[17] and its presence in the signal pathway is also reasonable. The signal transmission pathway is different in the bPAC-Y7F variant due to the absence of hydrogen bond interactions between Phe7 and Gln49.

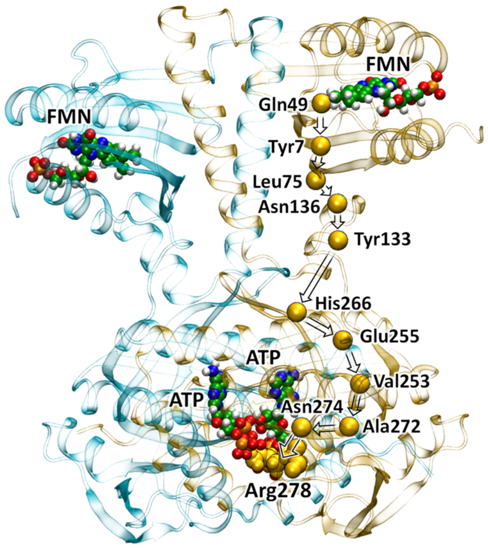

Figure 4. Amino acid residues involved in the signaling paths from Gln49 to Arg278 in bPAC. The nodes are shown as yellow balls. The Arg278 residue is shown in yellow space-filled spheres.

After leaving the BLUF domain, the signal pathway proceeds through Asn136 and Tyr133 from the handle of the protein complex and reaches the AC domain (Figure 4). Predominantly, the pathways proceed through the $\beta5_{AC}$ (His266) and $\beta4_{AC}$ (Val253 and Glu255). These β-sheets form the so-called tongue in the bPAC structure.[17] According to the X-ray studies, the His266 residue was found to be in different conformations in dark and light states that justifies its appearance in the signal pathway.[25] The Asn274 is the last intermediate point before reaching Arg278. The conformation of the side chain of Asn274 is different in the DS and LS (Figure 3, upper panel). In the LS, the amide group forms a stable hydrogen bond with the side chain of Arg278 and fixes it in the orientation closer to the substrate. In the DS, the Asn274 side chain is exposed to the protein surface and Arg278 becomes more flexible and more solvent-exposed. Thus, computationally derived signal transmission pathways between the Gln49 and Arg278 comprise amino acid residues, which presumably are involved in the signal transduction according to the analysis of the X-ray structures.[17]

Mechanism of the Chemical Reaction ATP → cAMP in the Dark and Light States. According to the classical MD simulations described above, the Arg278 side chain adopts two different conformations near the phosphate groups of ATP in the AC active site in the dark and light states of bPAC. The corresponding structures of the enzyme−substrate complexes, ES−DS and ES−LS, are illustrated in Figure 5. Initial coordinates of these structures were taken from the frames of classical MD trajectories; then, they were employed to launch the QM(DFT(ωB97X-D3/6-31G**))/MM(CHARMM) MD calculations. The guanidine group of Arg278 forms the hydrogen bonds with the oxygen atom of the ATP β-phosphate group in the ES−DS structure, whereas the Arg278 side chain is located near the α-phosphate group and forms the hydrogen bond with the O^{1A} atom of ATP in the

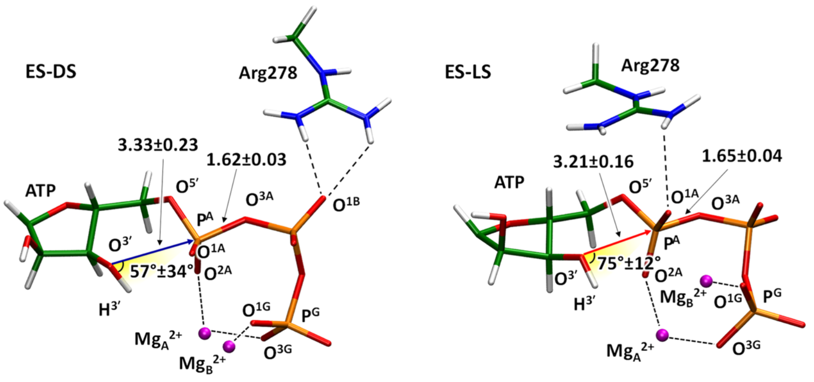

Figure 5. Fragments of the ES complexes in the dark (ES−DS, left) and light (ES−LS, right) states. Distances (in Å) and angles refer to the results of QM/MM MD calculations.

ES−LS structure (Figure 5). The values of interatomic distances and angles specified in Figure 5 refer to the results of QM/MM MD simulations. They illustrate the pronounced differences of the important geometry parameters in the DS and LS.

A nucleophilic attack of the $O^{3'}$ atom of the ribose group on the P^A atom following proton transfer from $O^{3'}H^{3'}$ is the key issue in the ATP → cAMP reaction in ACs. The upper panel in Figure 6 shows the distribution of the $O^{3'}-P^A$ distances in ES−DS (blue line) and ES−LS (red line) obtained in QM/MM MD simulations. In the ES−LS case, this distribution is narrower and it is shifted to smaller values as compared with the distribution in ES−DS. This is a strong indication that the nucleophilic attack should occur more readily in the ES−LS structure.

Two more panels in Figure 6 illustrate distributions of other geometry parameters in the ES complexes along QM/MM MD trajectories, which are important for the reaction. As we noted in the Introduction, previous modeling of AC catalysis[34−37] using different versions of the QM/MM method does not fully agree in details of the mechanism. Specifically, a candidate for the general base to accept the proton from the ribose group $O^{3'}H^{3'}$ of ATP (see Figure 1) is indicated differently in previous studies. Looking ahead, we claim that in the present simulations, the $H^{3'}$ proton is transferred to Asp157 via a water molecule coordinated by Mg_A^{2+}. This is a mechanism similar to that described in the most recent computational study of the mammalian ACs.[34] Examination of geometry parameters in the ES complexes and analysis of the Laplacian of electron density maps shown in Figure 7 provide a sound support to this reaction pathway.

The middle panel in Figure 6 illustrates distribution of the $\angle(P^A...O^{3'}-H^{3'})$ angle in ES−DS (blue line) and ES−LS (red line). The distribution for the ES−LS structure shows a single maximum at around 80°. In this conformation, $H^{3'}$ is hydrogen-bonded to the water molecule that may serve as a proton transfer shuttle to either Asp157 or Asp201 (see Figure 2). In ES−DS, the corresponding peak is much smaller and the major conformation refers to the value of $\angle(P^A...O^{3'}-H^{3'})$ at around 30°. In this case, $H^{3'}$ forms a hydrogen bond with the O^{1A} atom. These distributions emphasize an important role of the Arg278 conformation. In the LS, a stable hydrogen bond is formed between Arg278 and O^{1A} that prevents formation of the $H^{3'}\cdots O^{1A}$ hydrogen bond. In the DS, $H^{3'}$ forms a hydrogen bond with either O^{1A} or with a water molecule along the MD trajectory. Formation of the $H^{3'}\cdots O^{1A}$ hydrogen bond in the ES−DS leads to the following features. First, the distance of the nucleophilic attack increases. Second, an unfavorable orientation of the electron lone pair on the $O^{3'}$ atom responsible for the nucleophilic attack is observed in the Laplacian of electron density maps (Figure 7).

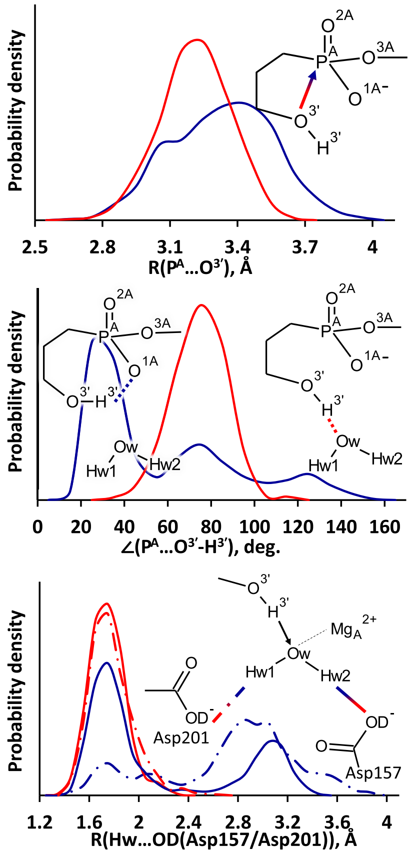

Figure 6. Distributions of geometry parameters in the enzyme−substrate complexes in the dark (ES−DS, blue) and light (ES−LS, red) states as obtained in QM/MM MD calculations. The upper panel illustrates the distributions of the distances of the nucleophilic attack. The middle panel shows the distributions of the angles between the $O^{3'}-H^{3'}$ bond and the direction of the nucleophilic attack. The lower panel shows distributions of hydrogen bond lengths between a hydrogen atom (Hw1 or Hw2) of the water molecule, Hw, and the oxygen atoms, OD, of the carboxyl group of Asp157 (solid line) and Asp201 (dash-dotted line).

If a conformation favors the nucleophilic attack, the electron lone pair in $O^{3'}$ (highlighted in magenta in the upper panel in

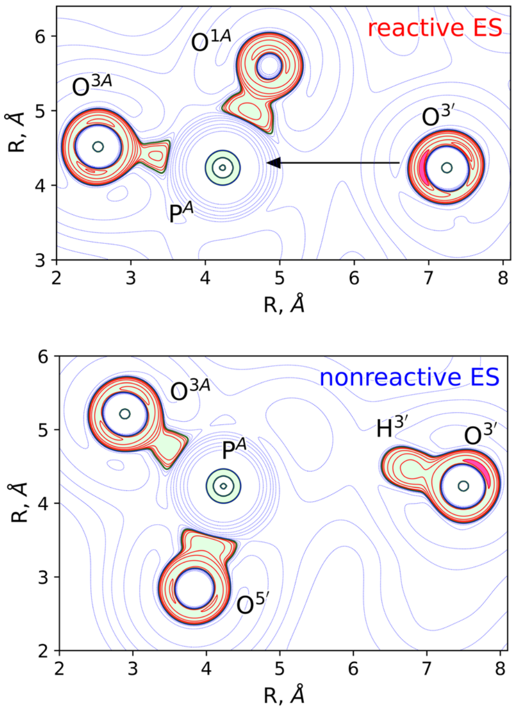

Figure 7. Laplacian of electron density in the plane formed by the nucleophile, the oxygen atom $\mathrm{O}^{3'}$, and the O^{3A}–P^{A} group of ATP. The upper panel shows the graph for the reactive ES; lower panel—graph for the nonreactive ES. Contour lines are $\pm(2;4;8)\cdot 10^{n}$ au, $-2 \leq n \leq 1$, blue-dashed contour lines indicate the electron density depletion areas ($\nabla^2\rho(\mathbf{r}) > 0$), red solid lines identify the electron density concentration ($\nabla^2\rho(\mathbf{r}) < 0$), and the green solid line corresponds to $\nabla^2\rho(\mathbf{r}) = 0$. The area with $\nabla^2\rho(\mathbf{r}) < 0$ is colored in light green and the lone pair on the oxygen atom $\mathrm{O}^{3'}$ is highlighted in magenta ($\nabla^2\rho(\mathbf{r}) < -4$).

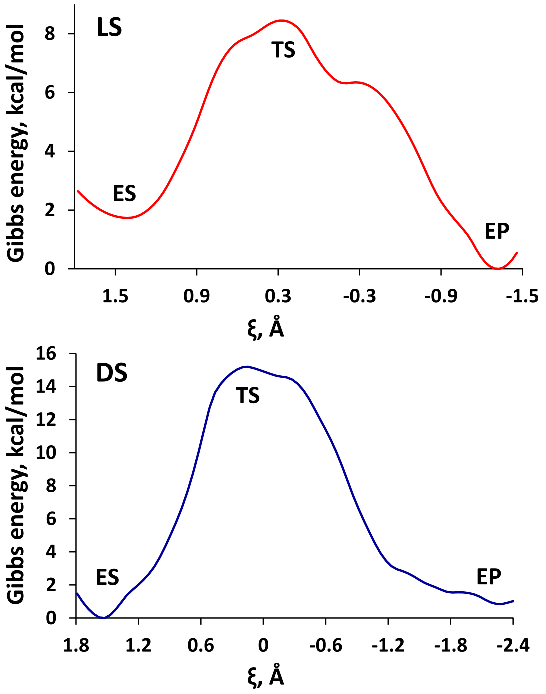

Figure 8. Gibbs energy profiles of the ATP → cAMP reaction computed in the QM(DFT(ωB97X-D3/6-31G**))/MM-(CHARMM) MD simulations. The upper panel refers to the light state; the bottom panel—the dark state.

Figure 7) is oriented toward the electrophilic P^{A} atom. Following the previous studies of nucleophile reactions,[39,40] we denote such complexes as "reactive ES". Contrary, if a $\mathrm{H}^{3'}\ldots\mathrm{O}^{1A}$ hydrogen bond is formed (Figure 6), the electron lone pair shown in the bottom panel in Figure 7 (highlighted in magenta) is oriented to the opposite side from the P^{A} atom. This corresponds to "nonreactive ES" complexes.

Other important geometry parameters favoring the chemical reaction are the hydrogen bonds that facilitate the $\mathrm{H}^{3'}$ transfer to one of the aspartates. A water molecule that is hydrogen-bonded to the $\mathrm{H}^{3'}$ atom serves as a hydrogen bond shuttle to carboxylates of the aspartate residues, Asp157 and Asp201. From the qualitative side, both of them are candidates to accept a proton during the reaction. We analyze the stability of both of these hydrogen bonds (Figure 6, lower panel). In the ES–LS trajectory, both hydrogen bonds are formed during the simulation. In the ES–DS, the dynamics is different; the fraction of the frames with both hydrogen bonds is about 5%, whereas only one of the hydrogen bonds is predominantly formed.

Results of these mostly qualitative considerations are perfectly consistent with the conclusions obtained in the straightforward calculations of the reaction energy profiles using the QM(DFT(ωB97X-D3/6-31G**))/MM-(CHARMM) MD simulations. The Gibbs energy profiles shown in Figure 8 are computed along the reaction coordinate ξ defined as a difference between the P^{A}–$\mathrm{O}^{3'}$ and O^{3A}–P^{A} distances. It is positive in the ES region and negative in the EP region. The ES minima are located at the ξ values of 1.4 and 1.5 Å for the LS and DS systems, respectively. The complex reaction coordinate (collective variable) does not provide information on the individual geometry parameters; therefore, we extracted values of the nucleophilic attack distances from the QM/MM MD simulations of the ES complexes. They are 3.21 ± 0.16 and 3.33 ± 0.23 Å for the ES–LS and ES–DS, respectively, indicating that the ES complex is tighter in the light state (Figure 5). The energy barrier of the nucleophilic attack is much lower in the LS, being 8.4 kcal/mol as compared with the DS case with the computed barrier of 15.4 kcal/mol. In both pathways, the $\mathrm{H}^{3'}$ proton is transferred to a water molecule and the latter transfers its proton to Asp157 (Figure 9). Our simulations demonstrate that the chemical step of the reaction is more accelerated in the light state as compared with the experimental steady-state kinetic data.[16,17] We emphasize that these experiments cannot firmly assign whether these data refer to the chemical step or other processes in this complex system. We think that in the dark state, the chemical reaction is the rate-limiting step, whereas in the light state, the product release may be the slowest process. This is in line with the experimental observations in mAC with the comparable rate constants of the PPi release and chemical reaction.[26]

Figure 9 illustrates the mechanism of the ATP → cAMP reaction in bPAC revealed in the present simulations. It shares common features with that in the mammalian AC,[34] including proton transfer from the ribose $\mathrm{O}^{3'}\mathrm{H}^{3'}$ group to the nearby aspartic acid via a shuttling water molecule concerted with P^{A}–O^{3A} bond cleavage and $\mathrm{O}^{3'}$–P^{A} bond formation.

We emphasize an important role of switching between conformations with different positions of Arg278 in the dark and light states of the system. In the LS, Arg278 forms a hydrogen bond with the O^{1A} atom in the reactants and forms

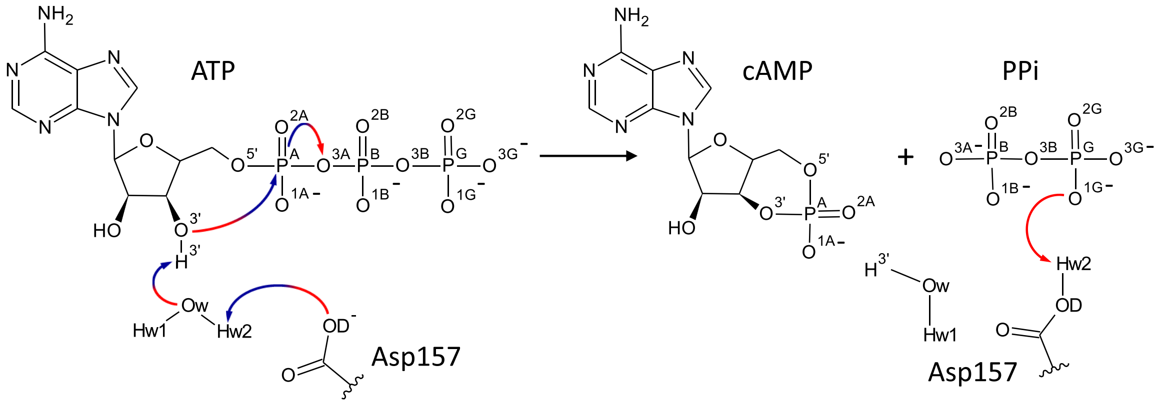

Figure 9. Reaction mechanism of the ATP hydrolysis in the active site of the catalytic domain of bPAC. The blue-red arrows depict the processes occurring in both the DS and LS. The red arrow in the right part corresponds to the process occurring only in the LS.

an additional hydrogen bond with the O^{3A} atom in the area of the TS (transition state) that stabilizes the latter. In the DS, Arg278 interacts with the PPi fragment obtained from the β- and γ-phosphates of the initial ATP molecule. The conformation of Arg278 in the light state also contributes to a lower energy of EP relative to ES by about 2 kcal/mol. The reaction pathway in the dark state does not show EP stabilization relative to ES.

One more role of the Arg278 conformations is in protonation of the PPi moiety after formation of EP, which should facilitate the release of PPi from the active site. In the LS, PPi ($P_2O_7^{4-}$) is stabilized by a hydrogen bond with the positively charged Arg284 and by three coordination bonds with the magnesium cations. This configuration facilitates proton transfer from Asp157 to the oxygen atom of the γ-phosphate group. In the DS, the PPi is stabilized by two additional hydrogen bonds with Arg278 and simultaneous proton transfer does not occur. We attempted to compute the Gibbs energy profile of the proton transfer in the DS; however, we failed to localize a minimum energy point with the proton forming a covalent bond with the PPi.

It should be noted that here, we analyze only the intrinsic chemical reaction ATP → cAMP + PPi that proceeds between the ES and EP points inside the protein cavity. The measured steady-state reaction rate constant in bPAC[17] refers to the complete set of processes including substrate deposition and product release besides the chemical step. Therefore, we can only speculate on the agreement between the experimental and theoretical results. However, what we definitely observe in molecular simulations is a considerable lowering of the chemical reaction energy barrier and formation of PPi in the protonation state, facilitating its release from the active site in the LS.

The significance of conformational changes in the side chain of the arginine residue in the enzyme active site in modulating the rate of the chemical reaction with ATP is not unexpected. The so-called arginine finger is well recognized in reactions of the enzyme-catalyzed phosphorus−oxygen bond cleavage in nucleotide triphosphate (NTP). The catalytically important Arg residue donated from external proteins to the active site can dramatically accelerate chemical reactions.[61−67] There are known examples of conformational changes in the arginine position due to formation of protein complexes, which lead to the manifold increase in the NTP hydrolysis rate constant.[68] These data support the idea proposed in the present study on the role of conformational changes of the side chain of Arg278 as an issue responsible for the acceleration of ATP to cAMP conversion.

■ CONCLUSIONS

The results of classical and QM/MM MD simulations of the wild-type and mutant photoactivated AC bPAC allow us to explain the mechanism of acceleration of the ATP to cAMP conversion in the catalytic AC domain after illumination of the photosensing BLUF domain. Following the dynamical network analysis, we recognize the signal transmission pathways from the chromophore environment to the AC active site. The 1 μs MD trajectories reveal the dynamical shift between conformations of the side chain of Arg278 near the phosphate groups of ATP in the active site of AC upon transformation from the dark state to the light state of the complex. Moreover, the corresponding distribution in arginine conformations in the bPAC-Y7F is intermediate between the dark and light states of the wild-type complex in agreement with the observed intermediate catalytic activity of the mutated form. We compare the Gibbs energy profiles of the chemical reaction computed at the QM/MM level with the *ab initio*-type potentials DFT(ωB97X-D3/6-31G**) in QM in the DS and LS systems. These profiles show a considerable lowering of the activation energy barrier due to the transformation from the dark state to the light state, which is qualitatively consistent with the experimentally detected increase in the reaction rate. The decrease in the reaction barrier in the light-activated system is due to a specific position of Arg278, which stabilizes pentacoordinated phosphorus of the α-phosphate group in the transition state. The disclosed mechanism of the reaction ATP → cAMP + PPi in the bPAC active site shares common features with that in the mammalian AC; it includes proton transfer from the ribose $O^{3\prime}H^{3\prime}$ group in ATP to the nearby aspartic acid via a shuttling water molecule concerted with P^A−O^{3A} bond cleavage and $O^{3\prime}$−P^A bond formation. We demonstrate that mapping the Laplacian of the electron density computed for the enzyme−substrate complexes in the AC active site provides easily visible images of the proper nucleophile orientation that allow us to distinguish between reactive and nonreactive ES structures. In summary, the results of these simulations for the first time describe a consistent picture of the photoinduced acceleration of the enzymatic reaction in bPAC.

AUTHOR INFORMATION

Corresponding Authors

Maria G. Khrenova − *Department of Chemistry, Lomonosov Moscow State University, Moscow 119991, Russian Federation; Bach Institute of Biochemistry, Federal Research Centre "Fundamentals of Biotechnology", Russian Academy of Sciences, Moscow 119071, Russian Federation;* orcid.org/0000-0001-7117-3089; Email: mkhrenova@lcc.chem.msu.ru

Alexander V. Nemukhin − *Department of Chemistry, Lomonosov Moscow State University, Moscow 119991, Russian Federation; Emanuel Institute of Biochemical Physics, Russian Academy of Sciences, Moscow 119334, Russian Federation;* orcid.org/0000-0002-4992-6029; Email: anem@lcc.chem.msu.ru

Author

Anna M. Kulakova − *Department of Chemistry, Lomonosov Moscow State University, Moscow 119991, Russian Federation*

Complete contact information is available at: https://pubs.acs.org/10.1021/acs.jcim.0c01308

Notes

The authors declare no competing financial interest.

ACKNOWLEDGMENTS

A.V.N. acknowledges support from the Russian Science Foundation (project #19-73-20032). We acknowledge the use of supercomputer resources of the Joint Supercomputer Center of the Russian Academy of Sciences and the equipment of the shared research facilities of HPC computing resources at Lomonosov Moscow State University.[69]

REFERENCES

(1) Losi, A.; Gardner, K. H.; Möglich, A. Blue-Light Receptors for Optogenetics. *Chem. Rev.* **2018**, *118*, 10659−10709.

(2) Schmermund, L.; Jurkaš, V.; Özgen, F. F.; Barone, G. D.; Büchsenschütz, H. C.; Winkler, C. K.; Schmidt, S.; Kourist, R.; Kroutil, W. Photo-Biocatalysis: Biotransformations in the Presence of Light. *ACS Catal.* **2019**, *9*, 4115−4144.

(3) Steuer Costa, W.; Yu, S.-c.; Liewald, J. F.; Gottschalk, A. Fast cAMP Modulation of Neurotransmission via Neuropeptide Signals and Vesicle Loading. *Curr. Biol.* **2017**, *27*, 495−507.

(4) Zhang, F.; Tzanakakis, E. S. Optogenetic Regulation of Insulin Secretion in Pancreatic β-Cells. *Sci. Rep.* **2017**, *7*, 9357.

(5) Luyben, T. T.; Rai, J.; Li, H.; Georgiou, J.; Avila, A.; Zhen, M.; Collingridge, G. L.; Tominaga, T.; Okamoto, K. Optogenetic Manipulation of Postsynaptic cAMP Using a Novel Transgenic Mouse Line Enables Synaptic Plasticity and Enhances Depolarization Following Tetanic Stimulation in the Hippocampal Dentate Gyrus. *Front. Neural Circuits* **2020**, *14*, 24.

(6) Blackburn, G. M.; Cherfils, J.; Moss, G. P.; Richards, N. G. J.; Waltho, J. P.; Williams, N. H.; Wittinghofer, A. How to Name Atoms in Phosphates, Polyphosphates, Their Derivatives and Mimics, and Transition State Analogues for Enzyme-Catalysed Phosphoryl Transfer Reactions (IUPAC Recommendations 2016). *Pure Appl. Chem.* **2017**, *89*, 653−675.

(7) Naim, N.; Reece, J. M.; Zhang, X.; Altschuler, D. L. Dual Activation of cAMP Production Through Photostimulation or Chemical Stimulation. In *Photoswitching Proteins*; Niopek, D., Ed.; Methods in Molecular Biology; Humana: New York, NY, 2020; pp 201−216.

(8) Khannpnavar, B.; Mehta, V.; Qi, C.; Korkhov, V. Structure and Function of Adenylyl Cyclases, Key Enzymes in Cellular Signaling. *Curr. Opin. Struct. Biol.* **2020**, *63*, 34−41.

(9) Bassler, J.; Schultz, J. E.; Lupas, A. N. Adenylate Cyclases: Receivers, Transducers, and Generators of Signals. *Cell. Signalling* **2018**, *46*, 135−144.

(10) Kobilka, B. The Structural Basis of G-Protein-Coupled Receptor Signaling (Nobel Lecture). *Angew. Chem., Int. Ed.* **2013**, *52*, 6380−6388.

(11) Ritter, J.; Flower, R.; Henderson, G.; Rang, H. *Rang & Dale's Pharmacology*, 8th ed.; Churchill Livingstone, 2015.

(12) Iwata, T.; Nagai, T.; Ito, S.; Osoegawa, S.; Iseki, M.; Watanabe, M.; Unno, M.; Kitagawa, S.; Kandori, H. Hydrogen Bonding Environments in the Photocycle Process around the Flavin Chromophore of the AppA-BLUF Domain. *J. Am. Chem. Soc.* **2018**, *140*, 11982−11991.

(13) Iseki, M.; Matsunaga, S.; Murakami, A.; Ohno, K.; Shiga, K.; Yoshida, K.; Sugai, M.; Takahashi, T.; Hori, T.; Watanabe, M. A Blue-Light-Activated Adenylyl Cyclase Mediates Photoavoidance in Euglena Gracilis. *Nature* **2002**, *415*, 1047−1051.

(14) Ohki, M.; Sato-Tomita, A.; Matsunaga, S.; Iseki, M.; Tame, J. R. H.; Shibayama, N.; Park, S.-Y. Molecular Mechanism of Photoactivation of a Light-Regulated Adenylate Cyclase. *Proc. Natl. Acad. Sci. U.S.A.* **2017**, *114*, 8562−8567.

(15) Ohki, M.; Sugiyama, K.; Kawai, F.; Tanaka, H.; Nihei, Y.; Unzai, S.; Takebe, M.; Matsunaga, S.; Adachi, S.-i.; Shibayama, N.; Zhou, Z.; Koyama, R.; Ikegaya, Y.; Takahashi, T.; Tame, J. R. H.; Iseki, M.; Park, S.-Y. Structural Insight into Photoactivation of an Adenylate Cyclase from a Photosynthetic Cyanobacterium. *Proc. Natl. Acad. Sci. U.S.A.* **2016**, *113*, 6659−6664.

(16) Ryu, M.-H.; Moskvin, O. V.; Siltberg-Liberles, J.; Gomelsky, M. Natural and Engineered Photoactivated Nucleotidyl Cyclases for Optogenetic Applications. *J. Biol. Chem.* **2010**, *285*, 41501−41508.

(17) Lindner, R.; Hartmann, E.; Tarnawski, M.; Winkler, A.; Frey, D.; Reinstein, J.; Meinhart, A.; Schlichting, I. Photoactivation Mechanism of a Bacterial Light-Regulated Adenylyl Cyclase. *J. Mol. Biol.* **2017**, *429*, 1336−1351.

(18) Stierl, M.; Stumpf, P.; Udwari, D.; Gueta, R.; Hagedorn, R.; Losi, A.; Gärtner, W.; Petereit, L.; Efetova, M.; Schwarzel, M.; Oertner, T. G.; Nagel, G.; Hegemann, P. Light Modulation of Cellular cAMP by a Small Bacterial Photoactivated Adenylyl Cyclase, bPAC, of the Soil Bacterium Beggiatoa. *J. Biol. Chem.* **2011**, *286*, 1181−1188.

(19) Penzkofer, A.; Stierl, M.; Hegemann, P.; Kateriya, S. Photo-Dynamics of the BLUF Domain Containing Soluble Adenylate Cyclase (nPAC) from the Amoeboflagellate Naegleria Gruberi NEG-M Strain. *Chem. Phys.* **2011**, *387*, 25−38.

(20) Blain-Hartung, M.; Rockwell, N. C.; Moreno, M. V.; Martin, S. S.; Gan, F.; Bryant, D. A.; Lagarias, J. C. Cyanobacteriochrome-Based Photoswitchable Adenylyl Cyclases (cPACs) for Broad Spectrum Light Regulation of cAMP Levels in Cells. *J. Biol. Chem.* **2018**, *293*, 8473−8483.

(21) Scheib, U.; Broser, M.; Constantin, O. M.; Yang, S.; Gao, S.; Mukherjee, S.; Stehfest, K.; Nagel, G.; Gee, C. E.; Hegemann, P. Rhodopsin-Cyclases for Photocontrol of cGMP/cAMP and 2.3 Å Structure of the Adenylyl Cyclase Domain. *Nat. Commun.* **2018**, *9*, 2046.

(22) Fushimi, K.; Enomoto, G.; Ikeuchi, M.; Narikawa, R. Distinctive Properties of Dark Reversion Kinetics between Two Red/Green-Type Cyanobacteriochromes and Their Application in the Photoregulation of cAMP Synthesis. *Photochem. Photobiol.* **2017**, *93*, 681−691.

(23) Hirano, M.; Takebe, M.; Ishido, T.; Ide, T.; Matsunaga, S. The C-Terminal Region Affects the Activity of Photoactivated Adenylyl Cyclase from Oscillatoria Acuminata. *Sci. Rep.* **2019**, *9*, 20262.

(24) Stierl, M.; Penzkofer, A.; Kennis, J. T. M.; Hegemann, P.; Mathes, T. Key Residues for the Light Regulation of the Blue Light-Activated Adenylyl Cyclase from Beggiatoa Sp. *Biochemistry* **2014**, *53*, 5121−5130.

(25) Yuan, H.; Dragnea, V.; Wu, Q.; Gardner, K. H.; Bauer, C. E. Mutational and Structural Studies of the PixD BLUF Output Signal That Affects Light-Regulated Interactions with PixE. *Biochemistry* **2011**, *50*, 6365−6375.

(26) Dessauer, C. W.; Gilman, A. G. The Catalytic Mechanism of Mammalian Adenylyl Cyclase. *J. Biol. Chem.* **1997**, *272*, 27787−27795.

(27) Tesmer, J. J.; Sunahara, R. K.; Gilman, A. G.; Sprang, S. R. Crystal Structure of the Catalytic Domains of Adenylyl Cyclase in a Complex with Gs·GTPS. *Science* **1997**, *278*, 1907−1916.

(28) Domratcheva, T.; Grigorenko, B. L.; Schlichting, I.; Nemukhin, A. V. Molecular Models Predict Light-Induced Glutamine Tautomerization in BLUF Photoreceptors. *Biophys. J.* **2008**, *94*, 3872−3879.

(29) Domratcheva, T.; Hartmann, E.; Schlichting, I.; Kottke, T. Evidence for Tautomerisation of Glutamine in BLUF Blue Light Receptors by Vibrational Spectroscopy and Computational Chemistry. *Sci. Rep.* **2016**, *6*, 22669.

(30) Grigorenko, B. L.; Khrenova, M. G.; Nemukhin, A. V. Amide-Imide Tautomerization in the Glutamine Side Chain in Enzymatic and Photochemical Reactions in Proteins. *Phys. Chem. Chem. Phys.* **2018**, *20*, 23827−23836.

(31) Khrenova, M. G.; Nemukhin, A. V.; Domratcheva, T. Photoinduced Electron Transfer Facilitates Tautomerization of the Conserved Signaling Glutamine Side Chain in BLUF Protein Light Sensors. *J. Phys. Chem. B* **2013**, *117*, 2369−2377.

(32) Goings, J. J.; Hammes-Schiffer, S. Early Photocycle of Slr1694 Blue-Light Using Flavin Photoreceptor Unraveled through Adiabatic Excited-State Quantum Mechanical/Molecular Mechanical Dynamics. *J. Am. Chem. Soc.* **2019**, *141*, 20470−20479.

(33) Goings, J. J.; Li, P.; Zhu, Q.; Hammes-Schiffer, S. Formation of an Unusual Glutamine Tautomer in a Blue Light Using Flavin Photocycle Characterizes the Light-Adapted State. *Proc. Natl. Acad. Sci. U.S.A.* **2020**, *117*, 26626.

(34) Grigorenko, B.; Polyakov, I.; Nemukhin, A. Mechanisms of ATP to cAMP Conversion Catalyzed by the Mammalian Adenylyl Cyclase: A Role of Magnesium Coordination Shells and Proton Wires. *J. Phys. Chem. B* **2020**, *124*, 451−460.

(35) Mones, L.; Tang, W.-J.; Florián, J. Empirical Valence Bond Simulations of the Chemical Mechanism of ATP to cAMP Conversion by Anthrax Edema Factor. *Biochemistry* **2013**, *52*, 2672−2682.

(36) Hahn, D. K.; Tusell, J. R.; Sprang, S. R.; Chu, X. Catalytic Mechanism of Mammalian Adenylyl Cyclase: A Computational Investigation. *Biochemistry* **2015**, *54*, 6252−6262.

(37) Jara, G. E.; Martínez, L. Anthrax Edema Factor: An Ion-Adaptive Mechanism of Catalysis with Increased Transition-State Conformational Flexibility. *J. Phys. Chem. B* **2016**, *120*, 6504−6514.

(38) Carroll, M. T.; Cheeseman, J. R.; Osman, R.; Weinstein, H. Nucleophilic Addition to Activated Double Bonds: Predictions of Reactivity from the Laplacian of the Charge Density. *J. Phys. Chem.* **1989**, *93*, 5120−5123.

(39) Khrenova, M. G.; Tsirelson, V. G.; Nemukhin, A. V. Dynamical Properties of Enzyme−Substrate Complexes Disclose Substrate Specificity of the SARS-CoV-2 Main Protease as Characterized by the Electron Density Descriptors. *Phys. Chem. Chem. Phys.* **2020**, *22*, 19069−19079.

(40) Khrenova, M. G.; Nemukhin, A. V.; Tsirelson, V. G. Discrimination of Enzyme−Substrate Complexes by Reactivity Using the Electron Density Analysis: Peptide Bond Hydrolysis by the Matrix Metalloproteinase-2. *Mendeleev Commun.* **2020**, *30*, 583−585.

(41) Word, J. M.; Lovell, S. C.; Richardson, J. S.; Richardson, D. C. Asparagine and Glutamine: Using Hydrogen Atom Contacts in the Choice of Side-Chain Amide Orientation. *J. Mol. Biol.* **1999**, *285*, 1735−1747.

(42) Kleinboelting, S.; van den Heuvel, J.; Steegborn, C. Structural Analysis of Human Soluble Adenylyl Cyclase and Crystal Structures of Its Nucleotide Complexes - Implications for Cyclase Catalysis and Evolution. *FEBS J.* **2014**, *281*, 4151−4164.

(43) Best, R. B.; Zhu, X.; Shim, J.; Lopes, P. E. M.; Mittal, J.; Feig, M.; MacKerell, A. D. Optimization of the Additive CHARMM All-Atom Protein Force Field Targeting Improved Sampling of the Backbone ϕ, ψ and Side-Chain χ_1 and χ_2 Dihedral Angles. *J. Chem. Theory Comput.* **2012**, *8*, 3257−3273.

(44) Denning, E. J.; Priyakumar, U. D.; Nilsson, L.; Mackerell, A. D. Impact of 2′-Hydroxyl Sampling on the Conformational Properties of RNA: Update of the CHARMM All-Atom Additive Force Field for RNA. *J. Comput. Chem.* **2011**, *32*, 1929−1943.

(45) Jorgensen, W. L.; Chandrasekhar, J.; Madura, J. D.; Impey, R. W.; Klein, M. L. Comparison of Simple Potential Functions for Simulating Liquid Water. *J. Chem. Phys.* **1983**, *79*, 926−935.

(46) Vanommeslaeghe, K.; Hatcher, E.; Acharya, C.; Kundu, S.; Zhong, S.; Shim, J.; Darian, E.; Guvench, O.; Lopes, P.; Vorobyov, I.; Mackerell, A. D. CHARMM General Force Field (CGenFF): A Force Field for Drug-like Molecules Compatible with the CHARMM All-Atom Additive Biological Force Fields. *J. Comput. Chem.* **2009**, *31*, 671−690.

(47) Khrenova, M. G.; Meteleshko, Y. I.; Nemukhin, A. V. Mutants of the Flavoprotein iLOV as Prospective Red-Shifted Fluorescent Markers. *J. Phys. Chem. B* **2017**, *121*, 10018−10025.

(48) Khrenova, M. G.; Domratcheva, T.; Schlichting, I.; Grigorenko, B. L.; Nemukhin, A. V. Computational Characterization of Reaction Intermediates in the Photocycle of the Sensory Domain of the AppA Blue Light Photoreceptor. *Photochem. Photobiol.* **2011**, *87*, 564−573.

(49) Humphrey, W.; Dalke, A.; Schulten, K. VMD: Visual Molecular Dynamics. *J. Mol. Graphics* **1996**, *14*, 33−38.

(50) Phillips, J. C.; Braun, R.; Wang, W.; Gumbart, J.; Tajkhorshid, E.; Villa, E.; Chipot, C.; Skeel, R. D.; Kalé, L.; Schulten, K. Scalable Molecular Dynamics with NAMD. *J. Comput. Chem.* **2005**, *26*, 1781−1802.

(51) Kots, E. D.; Khrenova, M. G.; Nemukhin, A. V. Allosteric Control of N-Acetyl-Aspartate Hydrolysis by the Y231C and F295S Mutants of Human Aspartoacylase. *J. Chem. Inf. Model.* **2019**, *59*, 2299−2308.

(52) Sethi, A.; Eargle, J.; Black, A. A.; Luthey-Schulten, Z. Dynamical Networks in TRNA:Protein Complexes. *Proc. Natl. Acad. Sci. U.S.A.* **2009**, *106*, 6620−6625.

(53) Glykos, N. M. Software News and Updates Carma: A Molecular Dynamics Analysis Program. *J. Comput. Chem.* **2006**, *27*, 1765−1768.

(54) Melo, M. C. R.; Bernardi, R. C.; Rudack, T.; Scheurer, M.; Riplinger, C.; Phillips, J. C.; Maia, J. D. C.; Rocha, G. B.; Ribeiro, J. V.; Stone, J. E.; Neese, F.; Schulten, K.; Luthey-Schulten, Z. NAMD Goes Quantum: An Integrative Suite for Hybrid Simulations. *Nat. Methods* **2018**, *15*, 351−354.

(55) Seritan, S.; Bannwarth, C.; Fales, B. S.; Hohenstein, E. G.; Isborn, C. M.; Kokkila-Schumacher, S. I. L.; Li, X.; Liu, F.; Luehr, N.; Snyder, J. W.; Song, C.; Titov, A. V.; Ufimtsev, I. S.; Wang, L. P.; Martínez, T. J. TeraChem: A Graphical Processing Unit-Accelerated Electronic Structure Package for Large-Scale Ab Initio Molecular Dynamics. *Wiley Interdiscip. Rev.: Comput. Mol. Sci.* **2020**, *11*, e1494.

(56) Matta, C. F.; Bader, R. F. W. Atoms-in-Molecules Study of the Genetically Encoded Amino Acids. III. Bond and Atomic Properties and Their Correlations with Experiment Including Mutation-Induced Changes in Protein Stability and Genetic Coding. *Proteins: Struct., Funct., Bioinf.* **2003**, *52*, 360−399.

(57) Khrenova, M. G.; Kulakova, A. M.; Nemukhin, A. V. Proof of Concept for Poor Inhibitor Binding and Efficient Formation of Covalent Adducts of KRAS G12C and ARS Compounds. *Org. Biomol. Chem.* **2020**, *18*, 3069−3081.

(58) Khrenova, M. G.; Krivitskaya, A. V.; Tsirelson, V. G. The QM/MM-QTAIM Approach Reveals the Nature of the Different Reactivity of Cephalosporins in the Active Site of L1 Metallo-β-Lactamase. *New J. Chem.* **2019**, *43*, 7329−7338.

(59) Lu, T.; Chen, F. Multiwfn: A Multifunctional Wavefunction Analyzer. *J. Comput. Chem.* **2012**, *33*, 580−592.

(60) Prah, A.; Purg, M.; Stare, J.; Vianello, R.; Mavri, J. How Monoamine Oxidase A Decomposes Serotonin: An Empirical Valence

Bond Simulation of the Reactive Step. *J. Phys. Chem. B* **2020**, *124*, 8259−8265.

(61) Nagy, G. N.; Suardíaz, R.; Lopata, A.; Ozohanics, O.; Vékey, K.; Brooks, B. R.; Leveles, I.; Tóth, J.; Vértessy, B. G.; Rosta, E. Structural Characterization of Arginine Fingers: Identification of an Arginine Finger for the Pyrophosphatase dUTPases. *J. Am. Chem. Soc.* **2016**, *138*, 15035−15045.

(62) Hayashi, S.; Ueno, H.; Shaikh, A. R.; Umemura, M.; Kamiya, M.; Ito, Y.; Ikeguchi, M.; Komoriya, Y.; Iino, R.; Noji, H. Molecular Mechanism of ATP Hydrolysis in F_1-ATPase Revealed by Molecular Simulations and Single-Molecule Observations. *J. Am. Chem. Soc.* **2012**, *134*, 8447−8454.

(63) Rydzek, S.; Shein, M.; Bielytskyi, P.; Schütz, A. K. Observation of a Transient Reaction Intermediate Illuminates the Mechanochemical Cycle of the AAA-ATPase P97. *J. Am. Chem. Soc.* **2020**, *142*, 14472−14480.

(64) Hanson, P. I.; Whiteheart, S. W. AAA+ Proteins: Have Engine, Will Work. *Nat. Rev. Mol. Cell Biol.* **2005**, *6*, 519−529.

(65) Gasper, R.; Meyer, S.; Gotthardt, K.; Sirajuddin, M.; Wittinghofer, A. It Takes Two to Tango: Regulation of G Proteins by Dimerization. *Nat. Rev. Mol. Cell Biol.* **2009**, *10*, 423−429.

(66) Calixto, A. R.; Moreira, C.; Pabis, A.; Kötting, C.; Gerwert, K.; Rudack, T.; Kamerlin, S. C. L. GTP Hydrolysis Without an Active Site Base: A Unifying Mechanism for Ras and Related GTPases. *J. Am. Chem. Soc.* **2019**, *141*, 10684−10701.

(67) Ahmadian, M. R.; Stege, P.; Scheffzek, K.; Wittinghofer, A. Confirmation of the Arginine-Finger Hypothesis for the GAP-Stimulated GTP-Hydrolysis Reaction of Ras. *Nat. Struct. Biol.* **1997**, *4*, 686−689.

(68) Mann, D.; Teuber, C.; Tennigkeit, S. A.; Schröter, G.; Gerwert, K.; Kötting, C. Mechanism of the Intrinsic Arginine Finger in Heterotrimeric G Proteins. *Proc. Natl. Acad. Sci. U.S.A.* **2016**, *113*, E8041−E8050.

(69) Voevodin, V. V.; Antonov, A. S.; Nikitenko, D. A.; Shvets, P. A.; Sobolev, S. I.; Sidorov, I. Y.; Stefanov, K. S.; Voevodin, V. V.; Zhumatiy, S. A. Supercomputer Lomonosov-2: Large Scale, Deep Monitoring and Fine Analytics for the User Community. *Supercomput. Front. Innov.* **2019**, *6*, 4−11.